J. Fluid Mech. (2014), *vol.* 756, *pp.* 226–251. © Cambridge University Press 2014
doi:10.1017/jfm.2014.403

Longitudinal–transverse aerodynamic force in viscous compressible complex flow

L. Q. Liu[1], Y. P. Shi[1,†], J. Y. Zhu[1], W. D. Su[1], S. F. Zou[1] and J. Z. Wu[1]

[1]State Key Laboratory of Turbulence and Complex System, College of Engineering, Peking University, Beijing 100871, PR China

(Received 26 September 2013; revised 10 July 2014; accepted 10 July 2014; first published online 1 September 2014)

We report our systematic development of a general and exact theory for diagnosis of total force and moment exerted on a generic body moving and deforming in a calorically perfect gas. The total force and moment consist of a longitudinal part (L-force) due to compressibility and irreversible thermodynamics, and a transverse part (T-force) due to shearing. The latter exists in incompressible flow but is now modulated by the former. The theory represents a full extension of a unified incompressible diagnosis theory of the same type developed by J. Z. Wu and coworkers to compressible flow, with Mach number ranging from low-subsonic to moderate-supersonic flows. Combined with computational fluid dynamics (CFD) simulation, the theory permits quantitative identification of various complex flow structures and processes responsible for the forces, and thereby enables rational optimal configuration design and flow control. The theory is confirmed by a numerical simulation of circular-cylinder flow in the range of free-stream Mach number M_∞ between 0.2 and 2.0. The L-drag and T-drag of the cylinder vary with M_∞ in different ways, the underlying physical mechanisms of which are analysed. Moreover, each L-force and T-force integrand contains a universal factor of local Mach number M. Our preliminary tests suggest that the possibility of finding new similarity rules for each force constituent could be quite promising.

Key words: aerodynamics, compressible flows, vortex flows

1. Introduction

1.1. *General background*

A vortical flow generated by a body moving through a fluid reacts to the body through the distributed stresses, total force and moment that it exerts. As a direct consequence of Newton's third law, the primary expressions for aerodynamic total force and moment take the form of surface-stress integrals. But most of the relevant physical mechanisms are not included in those 'standard' formulae. The underlying physics can be fully revealed in terms of three fundamental processes in fluid motion, namely the shearing process measured by vorticity, the compressing process measured by dilatation, pressure or some alternative thermodynamic variables, and the irreversible thermodynamics process (entropy process) measured by entropy

† Email address for correspondence: ypshi@coe.pku.edu.cn

https://doi.org/10.1017/jfm.2014.403 Published online by Cambridge University Press

variation (e.g. Lagerstrom, Cole & Trilling 1948; Kovásznay 1953; Wu 1956; Chu & Kovásznay 1958; Pierce 1989; Mao, Shi & Wu 2010; Mao *et al.* 2011), and their associated structures. Since it is only based on this deeper understanding that the body's geometry and motion can be rationally improved to obtain better performance, it is of significant value to further explore the specific physical mechanisms that cause a specific stress distribution on a body surface of given geometry and motion.

Ever since the pioneering works of the beginning of 20th century, great efforts have been made to develop fluid-dynamic force and moment theories by casting the surface-stress integrals into flow-field integrals via the momentum equation, and thereby revealing the contributions of local flow structures to the force and moment. We call the resulting incompressible theories 'vortical aerodynamics', the crucial mechanisms and related theories for which are summarized by two elegant theories on which the entire classic low-speed aerodynamic force–moment theory is based. One is the vortex-force theory for steady flow at the asymptotic limit of Reynolds number $Re \to \infty$ (Prandtl 1918, see also Saffman 1992), of which the two-dimensional Kutta–Joukowski theorem is an exact corollary and Prandtl's three-dimensional lifting-line theory is a linearized approximation. The other is the impulse theory which expresses the force and moment by the rate of change of vortical impulse for unsteady flow at arbitrary Reynolds number (Burgers 1921, also formulated by Wu 1981, independently and systematically), which has been used by von Kármán & Sears (1938) to construct a general linear theory for unsteady aerodynamics, with flutter theory as a special application. The Kármán–Sears theory has recently been extended to various three-dimensional and fully nonlinear unsteady aerodynamic problems (McCune & Tavares 1993; Wu 2007).

Classic aerodynamics theory, in pre-computer time, was focusing on solving the flow field as analytically as possible, and thus had to be mostly confined to thin wings and slender bodies at small angles of attack and large Reynolds numbers, so that the flow would remain fully attached and it would suffice to solve a global inviscid and irrotational flow by various approximations, along with thin boundary layers as well as highly simplified flat free vortex layers and straight vortex filaments to account for their influence on aerodynamic performance. Accordingly, the force and moment formulae were significantly simplified.

It has been a common task of modern aerodynamics, however, to deal with fluid reaction to a body of generic shape that may perform arbitrary motion and deformation. The body motion and deformation may generate a complicated unsteady, separated, and turbulent flow that may involve highly nonlinear and unsteady motion and interaction of various localized flow structures. The high nonlinearity inherent therein cannot be handled by any analytical approaches. But aerodynamicists can now rely on computational fluid dynamics (CFD) and advanced experimental techniques to obtain complex flow data for a better diagnosis to identify the couplings of the aforementioned three fundamental processes both in the interior of flow and on the boundary, to capture the key local flow structures (shear layers, vortices, shocks, etc.) and processes, and to find out how to rationally improve performance. Faced with a complex flow, it is even more desirable to have an exact theory that can explicitly bridge the aerodynamic performance and local flow structures. We call such a theory based on CFD data 'diagnosis theory'. In this direction, Wu, Ma & Zhou (2006) and Wu, Lu & Zhuang (2007) have unified vortex-force theory and impulse theory to form a complete, exact, and general formulation for the diagnosis of viscous and incompressible fluid-dynamic force and moment. Combined with CFD simulations, the unified theory has been applied to and confirmed by various engineering problems.

https://doi.org/10.1017/jfm.2014.403 Published online by Cambridge University Press

In contrast to these rich and powerful incompressible theories, corresponding exact theories for viscous compressible flows are relatively rare. Consequently, although in the past century the physical understanding of the key physical mechanisms involved in high-speed aerodynamics has been continuously enriched, such as transonic flow theory, the shock wave system and its interaction with a boundary layer, compressible turbulence, aeroacoustics, and aerodynamic heating, to name a few, no fully developed force–moment theory of field-integral type like incompressible vortical aerodynamics, and hence no complex flow diagnosis theory, has yet been available.

This paper reports our progress on a systematic investigation of fully extending the unified incompressible vortical aerodynamic force theory ('incompressible theory' for short) to compressible flows. Because the new theory is evolved from its incompressible version by exactly the same approach, it is appropriate here to briefly review the key points of the incompressible theory and previous efforts toward compressible theories.

1.2. *Main points of unified incompressible theory*

The incompressible theory is developed within a framework based on the so-called 'derivative-moment transformation' (DMT) (Wu *et al.* 2006). Two DMT identities to be used below are: in an n-dimensional space with $n = 2, 3$, the integrals of a vector field $\boldsymbol{f}$ and a scalar field ϕ can be cast as (see Wu *et al.* 2006, pp. 700–701)

$$\int_V \boldsymbol{f}\mathrm{d}V = \frac{1}{n-1}\int_V \boldsymbol{x}\times(\boldsymbol{\nabla}\times\boldsymbol{f})\mathrm{d}V - \frac{1}{n-1}\int_{\partial V}\boldsymbol{x}\times(\boldsymbol{n}\times\boldsymbol{f})\mathrm{d}S, \tag{1.1}$$

$$\int_S \phi\boldsymbol{n}\mathrm{d}S = -\frac{1}{n-1}\int_S \boldsymbol{x}\times(\boldsymbol{n}\times\boldsymbol{\nabla}\phi)\mathrm{d}S + \frac{1}{n-1}\oint_{\partial S}\phi\boldsymbol{x}\times\mathrm{d}\boldsymbol{x}, \tag{1.2}$$

where $\boldsymbol{x}$ is the position vector from an arbitrary fixed origin. These identities can transform the total force and moment in terms of standard surface-stress integrals into three equivalent forms, namely a boundary form in terms of the moments of boundary vorticity flux (BVF), a diffusion form in terms of the moments of $\mu\nabla^2\boldsymbol{\omega}$, and an advection form in terms of the Lamb vector $\boldsymbol{\omega}\times\boldsymbol{u}$, where $\boldsymbol{\omega} = \boldsymbol{\nabla}\times\boldsymbol{u}$ is vorticity. The boundary form can be conveniently applied to various flow diagnoses and optimal designs (see the review of Wu *et al.* 2009). The diffusion form has been used to identify the near-wall vortical flow structures directly responsible for pressure force and friction force (Wu *et al.* 2007; Fiabane, Gohlke & Cadot 2011). The advection form has been used to diagnose slender delta wing flow (Yang *et al.* 2007) and insect flight (Li & Lu 2012). It also provides a natural classification of aerodynamic force constituents by volume and boundary integrals of the Lamb vector, which leads to general and rational definitions of induced drag and form drag (Wu *et al.* 2006). This classification has been numerically confirmed by Marongiu, Tognaccini & Ueno (2013). For turbulent unsteady flow, Marongiu & Tognaccini (2010) have showed that the Reynolds-averaged Navier–Stokes (RANS) form of the advection form keeps exactly the same form as in laminar flow, provided that all quantities in the formulae are simply replaced by their mean values. For a two-dimensional turbulent flow over an oscillating NACA-0012 airfoil at angles of attack representative of both attached and separated flows at Reynolds numbers of 10^6–10^7, the lift and drag computed by the RANS-advection form are consistent with standard formulae.

Specifically, consider a body B moving and deforming arbitrarily through a fluid at rest or with uniform velocity $\boldsymbol{U}$ at infinity. In a fluid domain V_f bounded externally by

https://doi.org/10.1017/jfm.2014.403 Published online by Cambridge University Press

a control surface Σ and internally by the body surface ∂B, the incompressible force is expressed as (Wu *et al.* 2006, pp. 618–619)

$$\begin{aligned}\boldsymbol{F} &= -\rho\int_{V_f}\boldsymbol{l}\mathrm{d}V-\frac{\rho}{n-1}\int_{\partial V_f}\boldsymbol{x}\times(\boldsymbol{n}\times\boldsymbol{l})\mathrm{d}S+\boldsymbol{F}_{\Sigma}\\ &\quad -\frac{\rho}{n-1}\int_{V_f}\boldsymbol{x}\times\boldsymbol{\omega}_{,t}\mathrm{d}V+\boldsymbol{F}_B \qquad (1.3a)\\ &= -\frac{\rho}{n-1}\int_{V_f}\boldsymbol{x}\times\mu\nabla^2\boldsymbol{\omega}\mathrm{d}V+\boldsymbol{F}_{\Sigma}+\boldsymbol{F}_B, \qquad (1.3b)\end{aligned}$$

where $\boldsymbol{l}=\boldsymbol{\omega}\times\boldsymbol{u}$ is the Lamb vector, $n=2,3$ is the spatial dimension, and

$$\begin{aligned}\boldsymbol{F}_{\Sigma} &= -\frac{\mu}{n-1}\int_{\Sigma}\boldsymbol{x}\times[\boldsymbol{n}\times(\nabla\times\boldsymbol{\omega})]\mathrm{d}S+\int_{\Sigma}\boldsymbol{\tau}\mathrm{d}S, \qquad (1.4a)\\ \boldsymbol{F}_B &= \frac{1}{n-1}\int_{\partial B}\boldsymbol{x}\times(\boldsymbol{n}\times\rho\boldsymbol{a}_B)\mathrm{d}S \qquad (1.4b)\end{aligned}$$

are the viscous force on Σ with $\boldsymbol{\tau}\equiv\mu\boldsymbol{\omega}\times\boldsymbol{n}$, and a body-surface integral with $\boldsymbol{a}_B$ denoting the acceleration on ∂B, respectively. Equations (1.3*a*) and (1.3*b*) are the advection and diffusion forms, respectively. Letting $V_f\to 0$ leads to the boundary form (Wu *et al.* 2006).

If we continue the velocity field $\boldsymbol{u}$ into the body B, which is allowed due to the adherence condition at ∂B, and denote $V=V_f+B$ as the volume enclosed by Σ, then we see the following.

First, for steady flow over a stationary body B the second line of (1.3*a*) vanishes, so the total force is almost solely expressed in terms of the Lamb vector:

$$\boldsymbol{F}=-\rho\int_{V}\boldsymbol{l}\mathrm{d}V-\frac{\rho}{n-1}\int_{\Sigma}\boldsymbol{x}\times(\boldsymbol{n}\times\boldsymbol{l})\mathrm{d}S+\boldsymbol{F}_{\Sigma}. \qquad (1.5)$$

As $Re\to\infty$, the Σ-integrals in (1.5) vanish, so it returns to the Prandtl (1918) classic vortex-force theory.

Second, owing to the kinematic identity

$$\vartheta\boldsymbol{u}+\boldsymbol{\omega}\times\boldsymbol{u}=\nabla\cdot\left(\boldsymbol{u}\boldsymbol{u}-\tfrac{1}{2}|\boldsymbol{u}|^2\boldsymbol{I}\right), \qquad (1.6)$$

where $\vartheta=\nabla\cdot\boldsymbol{u}$ is the dilatation, when $\vartheta=0$ and V extends to the entire space V_∞, there are three important Lamb vector integral properties:

$$\int_{V_\infty}\boldsymbol{\omega}\times\boldsymbol{u}\mathrm{d}V=0, \qquad (1.7a)$$

$$\int_{V_\infty}\boldsymbol{x}\times(\boldsymbol{\omega}\times\boldsymbol{u})\mathrm{d}V=0, \qquad (1.7b)$$

$$\int_{V_\infty}\boldsymbol{x}\cdot(\boldsymbol{\omega}\times\boldsymbol{u})\mathrm{d}V=(n-2)\int_{V_\infty}\frac{1}{2}|\boldsymbol{u}|^2\mathrm{d}V. \qquad (1.7c)$$

Thus, for unsteady flow with infinite domain V_∞ the remaining terms in (1.3) just yield the main formula of impulse theory

$$\boldsymbol{F}=-\rho\frac{\mathrm{d}\boldsymbol{I}_\infty}{\mathrm{d}t}+\rho\frac{\mathrm{d}}{\mathrm{d}t}\int_B\boldsymbol{u}\mathrm{d}V,\quad \boldsymbol{I}_\infty\equiv\frac{1}{n-1}\int_{V_\infty}\boldsymbol{x}\times\boldsymbol{\omega}\mathrm{d}V. \qquad (1.8)$$

Therefore, the classic vortex-force theory and impulse theory are two special cases of the unified theory under different conditions.

https://doi.org/10.1017/jfm.2014.403 Published online by Cambridge University Press

1.3. *Previous efforts toward compressible theory*

Oswatitsch (1956, p. 209) was the first to express the wave drag by the local entropy increment behind a shock, and thereby pioneered the present research direction. However, there was no further work on this for more than three decades until, motivated by interest turning from simple attached flow to compressible complex flow and by the development of CFD, new progress was made in the 1980s, mainly marked by the following advances.

First, within the framework of DMT, Wu and coworkers showed in a series of papers (Wu, Wu & Wu 1988; Wu & Wu 1993, 1996) that the boundary form of force–moment theory can be directly extended to compressible flows; this has played a significant role in the optimal design of transonic axial compressor blades (Wu *et al.* 2009). Meanwhile, the diffusion form of the force formula in terms of the moment of $\mu\nabla^2\boldsymbol{\omega}$, (1.3*b*), is also applicable to both incompressible and compressible flows (Wu & Wu 1993; Wu *et al.* 2007, 2010).

Secondly, Huang (1994) systematically generalized the impulse theory for unsteady aerodynamics to compressible flow, where the vorticity is replaced by a 'dynamic vorticity' $\boldsymbol{\omega}^* \equiv \boldsymbol{\nabla} \times (\rho\boldsymbol{u})$. Unfortunately, it is difficult to directly apply Huang's formulation to practical diagnosis of complex compressible flows.

Thirdly, the key object in developing compressible aerodynamics is to extend the advection form (1.3*a*) to compressible flow, since it can fully display the roles of three fundamental processes and associated flow structures in the entire flow field within an arbitrary finite analysis domain, as is mostly encountered in practical computations and experiments. In two distinct formulations of total-force formulae in terms of local dynamics, Chang, Su & Lei (1998) and Wu *et al.* (2006, p. 621) both found that the force formulae of the advection form for compressible flow can be obtained by simple replacements in the corresponding incompressible formulae:

$$\rho\boldsymbol{l} \Longrightarrow \rho\boldsymbol{l} - k\boldsymbol{\nabla}\rho, \quad \rho\boldsymbol{\omega}_{,t} \Longrightarrow \boldsymbol{\nabla} \times (\rho\boldsymbol{u}_{,t}), \tag{1.9a,b}$$

where

$$k \equiv \tfrac{1}{2}|\boldsymbol{u}|^2 \tag{1.10}$$

denotes the kinetic energy of fluid of unit mass. Thus, for steady flow (1.5) is extended to (if the viscous boundary integral $\boldsymbol{F}_\Sigma$ is negligible as in the case of $Re \gg 1$)

$$\boldsymbol{F} = \int_{V_f} (\rho\boldsymbol{u} \times \boldsymbol{\omega} + k\boldsymbol{\nabla}\rho)\mathrm{d}V + \frac{1}{n-1}\int_{\partial V_f} \boldsymbol{x} \times [\boldsymbol{n} \times (\rho\boldsymbol{u} \times \boldsymbol{\omega} + k\boldsymbol{\nabla}\rho)]\mathrm{d}S. \tag{1.11}$$

Numerical examples studied by Chang *et al.* (1998), Luo (2004), and Xu, Chen & Lu (2010) have shown that the extra term $k\boldsymbol{\nabla}\rho$ can indeed capture the compressibility effect. As free-stream Mach number M_∞ increases from zero, these authors found that the relative importance of the vortex force $\rho\boldsymbol{u} \times \boldsymbol{\omega}$ in (1.11) decreases and that of longitudinal force $k\boldsymbol{\nabla}\rho$ increases. The latter dominates the total force from high-subsonic to supersonic regimes.

Very recently, Mele & Tognaccini (2014) observed that, using (1.1), the integrals of $k\boldsymbol{\nabla}\rho$ in (1.11) can be transformed to a single volume integral of the moment of its curl, $\boldsymbol{\nabla} \times (k\boldsymbol{\nabla}\rho) = -\boldsymbol{\nabla} \times (\rho\boldsymbol{\nabla}k)$. They then proved that for steady flow this transformed integrand is non-zero only in boundary layers and the vortical wake behind curved shocks, and hence the compactness of the integrands of (1.11) is recovered. This formulation was confirmed by the authors' two-dimensional RANS

https://doi.org/10.1017/jfm.2014.403 Published online by Cambridge University Press

simulation of steady flow over a NACA-0012 airfoil. An interesting finding of their numerical results is that in subsonic and some low-transonic regimes the predicted lift is in good agreement with that predicted by the incompressible Kutta–Joukowski theorem, $L = \rho_\infty U_\infty \Gamma$, but the reason remains unclear. We remark that the DMT of the $k\nabla\rho$ term can be viewed as a part of an intermediate step toward our diffusion form (1.3*b*) for compressible flow (Wu *et al.* 2006, 2007, see also (2.9*b*) below).

1.4. *Our work and this paper*

Our work on developing compressible diagnosis theory moves forward from (1.11) and its unsteady version. The major results are:

(i) A dynamic generalization of the Lamb vector (generalized Lamb vector for short) suitable for studying aerodynamic force and moment has been found and proved to have exactly the same integral properties as (1.7) in free space. Consequently, a compressible unified theory follows simply from replacing the Lamb vector in the incompressible theory by this generalized version. Naturally, the new theory contains further compressible extensions of classic vortex-force theory and impulse theory as special cases.

(ii) For steady flow, the dynamic constituents of the term $k\nabla \ln \rho$ in (1.11) have been examined in terms of the aforementioned three fundamental processes in fluid motion. This leads to a splitting of the steady force into a longitudinal force (L-force) due to compressibility and thermodynamics, and a transverse force (T-force) due to shearing.

(iii) The LT-force theory has been extended to unsteady flow, which was confirmed by a high-fidelity numerical simulation of laminar flow over a two-dimensional circular cylinder with free-stream Mach number M_∞ ranging from 0.2 to 2.0. Since this flow is a typical spontaneously unsteady and separated flow with rich structures and interactions, it is an ideal example to display the wide capability of the new general theory.

(iv) The underlying physical mechanisms for the M_∞-dependence of time-averaged L-drag and T-drag of the cylinder were clarified by the coupling of the shearing and compressing–thermal processes both in the interior of fluid and on the cylinder surface.

(v) Each L-force and T-force integrand contains a universal factor of local Mach number M. Some preliminary tests were performed, suggesting that the possibility of finding new similarity rules for each force constituent could be quite promising.

The above results (i) and (ii) are reported in a companion paper (Liu *et al.* 2014). In this paper we focus on items (iii), (iv) and (v). In § 2 we develop a theory for unsteady compressible flow. Section 3 presents our numerical simulation of circular-cylinder flow and shows the computed flow patterns at different M_∞. Section 4 makes a diagnosis of the physics behind the M_∞-dependence of the L-drag and T-drag. Section 5 presents our tests in seeking for possible Mach-number similarity rules. Conclusions are made in § 6.

2. A theory of unsteady and compressible aerodynamic forces

We consider a body moving and deforming arbitrarily in a calorically perfect gas externally unbounded and at rest at infinity. The shear viscosity μ, longitudinal

https://doi.org/10.1017/jfm.2014.403 Published online by Cambridge University Press

viscosity μ_θ ($\mu_\theta = \zeta + (4/3)\mu$, where ζ is the bulk viscosity; in the following numerical calculations we will adopt the Stokes assumption $\zeta = 0$, so $\mu_\theta = (4/3)\mu$) and heat conductivity κ of the gas are temperature dependent, but we assume them constant solely for neatness at the present stage focusing on the development and testing of the new formulation. The continuity equation, Navier–Stokes (N–S) equation per unit volume, and energy equation read:

$$\frac{\mathrm{D}\rho}{\mathrm{D}t} = \rho_{,t} + \boldsymbol{u}\cdot\boldsymbol{\nabla}\rho = -\rho\vartheta, \tag{2.1a}$$

$$\rho\boldsymbol{a} = (\rho\boldsymbol{u})_{,t} + \boldsymbol{\nabla}\cdot(\rho\boldsymbol{u}\boldsymbol{u}) = -\boldsymbol{\nabla}\Pi - \boldsymbol{\nabla}\times(\mu\boldsymbol{\omega}), \tag{2.1b}$$

$$\rho T\frac{\mathrm{D}s}{\mathrm{D}t} = \Phi + \kappa\nabla^2 T, \tag{2.1c}$$

where $\Pi \equiv p - \mu_\theta\vartheta$ is the revised normal stress including viscous effects and $\Phi = \mu_\theta\vartheta^2 + \mu\omega^2 - \boldsymbol{\nabla}\cdot(2\mu\boldsymbol{B}\cdot\boldsymbol{u})$ is the dissipation rate, where $\boldsymbol{B} \equiv \vartheta\boldsymbol{I} - (\boldsymbol{\nabla}\boldsymbol{u})^{\mathrm{T}}$ is the surface deformation-rate tensor (Wu *et al.* 2006). We remark that this differential formulation for viscous and unsteady compressible flows is consistent with the mathematic properties of the Navier–Stokes equations, which are of parabolic type at all Mach numbers within the framework of continuum mechanics, having five families of characteristics and infinite signal-propagation speed (like the heat equation). Shock waves appear as thin viscous shock layers and are considered as 'sub-characteristics' (Lagerstrom *et al.* 1948). However, although a specially designed numerical method based on an exact theoretical Navier–Stokes solution can solve the thin viscous shock layer well (Gilbarg & Paolucci 1953; Sherman 1955), conventional CFD codes cannot. In making a diagnosis of CFD-based flow solutions using a theory, therefore, numerically identified shocks have to be treated as strong discontinuities satisfying Rankine–Hugoniot jump relations like in inviscid flow. This would involve replacing local differentiations and integrations by jumps of vorticity and dilatation, etc., across the shocks. We are now working on this subtle issue, but in this paper consider only the smooth-flow theory.

2.1. *Total force and moment*

The 'standard' formula for the total force $\boldsymbol{F}$ acting on the body is expressed in terms of a surface-stress integral:

$$\boldsymbol{F} = -\int_{\partial B}(-\Pi\boldsymbol{n} + \boldsymbol{\tau})\mathrm{d}S. \tag{2.2}$$

To transform it to a field integral able to exhibit dynamic processes and structures, we introduce the notation

$$K \equiv \tfrac{1}{2}\rho|\boldsymbol{u}|^2 = \rho k, \quad \Pi_0 \equiv \Pi + K, \quad \boldsymbol{m} \equiv \rho\boldsymbol{u}, \tag{2.3a–c}$$

and define a vector field

$$\rho\boldsymbol{f} \equiv \boldsymbol{\nabla}\cdot(\rho\boldsymbol{u}\boldsymbol{u} - K\boldsymbol{I}). \tag{2.4}$$

Since, $\boldsymbol{f} = \boldsymbol{\omega}\times\boldsymbol{u}$ for constant ρ Liu *et al.* (2014) call $\boldsymbol{f}$ a (dynamic) generalized Lamb vector. Then, subtracting $\boldsymbol{\nabla}K$ from both sides of (2.1*b*) yields

$$\boldsymbol{m}_{,t} + \rho\boldsymbol{f} = -\boldsymbol{\nabla}\Pi_0 - \boldsymbol{\nabla}\times(\mu\boldsymbol{\omega}), \tag{2.5}$$

https://doi.org/10.1017/jfm.2014.403 Published online by Cambridge University Press

so the integral momentum equation reads

$$\int_{V_f}(\boldsymbol{m}_{,t}+\rho\boldsymbol{f})\mathrm{d}V=\int_{\partial V_f}(-\Pi_0\boldsymbol{n}+\boldsymbol{\tau})\mathrm{d}S, \tag{2.6}$$

where $\partial V_f=\partial B+\Sigma$. Then, using (2.6) and DMT identities (1.1) and (1.2), we may cast (2.2) into a neat form:

$$\boldsymbol{F}=-\int_{V_f}\rho\boldsymbol{f}\mathrm{d}V-\frac{1}{n-1}\int_{\partial V_f}\boldsymbol{x}\times(\boldsymbol{n}\times\rho\boldsymbol{f})\mathrm{d}S+\boldsymbol{F}_\Sigma\frac{1}{n-1}\int_{V_f}\boldsymbol{x}\times\boldsymbol{\omega}^*_{,t}\mathrm{d}V+\boldsymbol{F}_B, \tag{2.7}$$

where $\boldsymbol{\omega}^*=\nabla\times\boldsymbol{m}$, and $\boldsymbol{F}_B$ and $\boldsymbol{F}_\Sigma$ are still given by (1.4*b*) and (1.4*a*), respectively.

Then, as suggested by (2.5), for a generic unsteady flow we define another vector field

$$\rho\boldsymbol{j}\equiv\boldsymbol{m}_{,t}+\rho\boldsymbol{f}=\rho\boldsymbol{a}-\nabla K, \tag{2.8}$$

and simply call $\boldsymbol{j}$ the longitudinal–transverse force per unit mass. The generalized Lamb vector is its steady version. Thus, (2.7) takes the form as a perfect counterpart of (1.3):

$$\boldsymbol{F}=-\int_{V_f}\rho\boldsymbol{j}\mathrm{d}V-\frac{1}{n-1}\int_{\partial V_f}\boldsymbol{x}\times(\boldsymbol{n}\times\rho\boldsymbol{j})\mathrm{d}S+\boldsymbol{F}_B+\boldsymbol{F}_\Sigma \tag{2.9a}$$

$$=-\frac{1}{n-1}\int_{V_f}\boldsymbol{x}\times[\nabla\times(\rho\boldsymbol{j})]\mathrm{d}V+\boldsymbol{F}_B+\boldsymbol{F}_\Sigma. \tag{2.9b}$$

Note that while (2.9*a*) is the desired advection form, (2.9*b*) is the diffusion form identical to (1.3*b*) since $\nabla\times(\rho\boldsymbol{j})=\nabla^2(\mu\boldsymbol{\omega})$. This reconfirms the direct applicability of (1.3*b*) to compressible flow.

The total moment can be similarly treated. Here we just list the result but omit the algebra:

$$\boldsymbol{M}=-\int_{V_f}\boldsymbol{x}\times\rho\boldsymbol{j}\mathrm{d}V+\frac{1}{2}\int_{\partial V_f}x^2(\boldsymbol{n}\times\rho\boldsymbol{j})\mathrm{d}S+\boldsymbol{M}_B+\boldsymbol{M}_\Sigma \tag{2.10a}$$

$$=\frac{1}{2}\int_{V_f}x^2\nabla\times(\rho\boldsymbol{j})\mathrm{d}V+\boldsymbol{M}_B+\boldsymbol{M}_\Sigma, \tag{2.10b}$$

where

$$\boldsymbol{M}_B=-\frac{1}{2}\int_{\partial B}x^2\boldsymbol{n}\times\rho\boldsymbol{a}_B\mathrm{d}S, \tag{2.11a}$$

$$\boldsymbol{M}_\Sigma=\frac{\mu}{2}\int_\Sigma x^2\boldsymbol{n}\times(\nabla\times\boldsymbol{\omega})\mathrm{d}S+\int_\Sigma\boldsymbol{x}\times\boldsymbol{\tau}\mathrm{d}S+\boldsymbol{M}_{s\Sigma}, \tag{2.11b}$$

$$\boldsymbol{M}_{s\Sigma}=-(n-1)\mu\int_\Sigma\boldsymbol{n}\times\boldsymbol{u}\mathrm{d}S=-(n-1)\mu\int_V\boldsymbol{\omega}\mathrm{d}V. \tag{2.11c}$$

Equation (2.9) is also exactly the counterpart of the incompressible moment formulae given in Wu *et al.* (2006, pp. 618–619).

https://doi.org/10.1017/jfm.2014.403 Published online by Cambridge University Press

2.2. *Effect of compressibility*

Our main concern below is to extract as much information as possible from (2.9*a*), focusing on the effects of flow compressibility.

From (2.4) we have

$$\begin{aligned}\rho \boldsymbol{f} &= \boldsymbol{\nabla}\cdot[\rho(\boldsymbol{uu}-k\boldsymbol{I})]=\rho[\boldsymbol{\nabla}\cdot(\boldsymbol{uu}-k\boldsymbol{I})]+(\boldsymbol{uu}-k\boldsymbol{I})\cdot\boldsymbol{\nabla}\rho\\ &= \rho[\vartheta\boldsymbol{u}+\boldsymbol{\omega}\times\boldsymbol{u}+(\boldsymbol{uu}-k\boldsymbol{I})\cdot\boldsymbol{\nabla}\ln\rho]\\ &= \rho[\boldsymbol{\omega}\times\boldsymbol{u}-(\boldsymbol{u}\partial_t+k\boldsymbol{\nabla})\ln\rho],\end{aligned} \tag{2.12}$$

where in the last step we used a consequence of the continuity equation

$$\boldsymbol{uu}\cdot\boldsymbol{\nabla}\rho=-\boldsymbol{u}(\rho_{,t}+\rho\vartheta). \tag{2.13}$$

Therefore, it follows that

$$\boldsymbol{f}=\boldsymbol{\omega}\times\boldsymbol{u}-(\boldsymbol{u}\partial_t+k\boldsymbol{\nabla})\ln\rho, \tag{2.14}$$

and, since $\boldsymbol{m}_{,t}=\boldsymbol{u}\rho_{,t}+\rho\boldsymbol{u}_{,t}$,

$$\boldsymbol{j}=\frac{1}{\rho}\boldsymbol{m}_{,t}+\boldsymbol{f}=\boldsymbol{u}_{,t}+\boldsymbol{\omega}\times\boldsymbol{u}-k\boldsymbol{\nabla}\ln\rho. \tag{2.15}$$

Substituting this into (2.9*a*), we see at once that for steady flow (1.11) is recovered when $\boldsymbol{F}_\Sigma$ is neglected. However, once we enter the unsteady flow regime, unlike incompressible unsteady flow, now $\boldsymbol{m}_{,t}$ and $\rho\boldsymbol{f}$ are no longer separable. Their inherent link via density unsteadiness is likely from the propagation of acoustic waves and shock waves, and their interactions with other flow structures.

Now, the last term of (2.15) can be written as

$$-k\boldsymbol{\nabla}\ln\rho=\frac{\gamma}{2}M^2p\boldsymbol{\nabla}\left(\frac{1}{\rho}\right),\quad \gamma=\frac{c_p}{c_v},\quad M\equiv\frac{|\boldsymbol{u}|}{a}, \tag{2.16a–c}$$

where a is the local sound speed. Then, letting $e=c_vT$ be the internal energy and $h=c_pT$ be the enthalpy, by the first law of thermodynamics,

$$\boldsymbol{\nabla}h=\boldsymbol{\nabla}e+p\boldsymbol{\nabla}\left(\frac{1}{\rho}\right)+\frac{1}{\rho}\boldsymbol{\nabla}p, \tag{2.17}$$

and using the momentum equation, we find

$$-k\boldsymbol{\nabla}\ln\rho=\frac{\gamma}{2}M^2[\boldsymbol{\nabla}(h_0-e)+\boldsymbol{u}_{,t}+\boldsymbol{\omega}\times\boldsymbol{u}-\boldsymbol{\eta}]. \tag{2.18}$$

Here,

$$\boldsymbol{\eta}\equiv\frac{1}{\rho}[\boldsymbol{\nabla}(\mu_\theta\vartheta)-\boldsymbol{\nabla}\times(\mu\boldsymbol{\omega})] \tag{2.19a}$$

is the viscous force of unit mass and

$$h_0-e=k+h-e=k+RT=\left(1+\frac{\gamma}{2}M^2\right)RT, \tag{2.19b}$$

https://doi.org/10.1017/jfm.2014.403 Published online by Cambridge University Press

with R being the gas const. Substituting (2.19*b*) into (2.18) and defining two local Mach-number factors

$$\alpha(M) \equiv 1 + \frac{\gamma}{2}M^2, \quad \beta(M) \equiv \frac{\gamma}{2}M^2, \tag{2.20a,b}$$

we have

$$-k\nabla \ln \rho = \beta(M)[\boldsymbol{u}_{,t} + \boldsymbol{\omega} \times \boldsymbol{u} + R\nabla(\alpha T) - \boldsymbol{\eta}]. \tag{2.21}$$

From (2.21) we see that although kinematically (along with the continuity equation) $k\nabla\rho$ appears as a purely compressibility effect, it actually has three dynamic sources from compressing, shearing, and entropy processes (the entropy process is absorbed into $\nabla(\alpha T)$). The physical reason for this multiple-process involvement is that the extra term $k\nabla\rho$ in the force has to be balanced by the gradient of thermodynamic pressure (which exists only in compressible flow and is proportional to γM^2) in the momentum equation (e.g. Lagerstrom 1964, p. 153); but in our formulation the pressure gradient is to be re-expressed by local flow structures as shown in (2.21). Therefore, (2.15) becomes

$$\boldsymbol{j} = \alpha(M)(\boldsymbol{u}_{,t} + \boldsymbol{\omega} \times \boldsymbol{u}) + \beta(M)[R\nabla(\alpha T) - \boldsymbol{\eta}]. \tag{2.22}$$

2.3. *LT-force constituents*

In order to display various processes completely, we first split the velocity field into a longitudinal part and a transverse part:

$$\boldsymbol{u} = \nabla\phi + \nabla \times \boldsymbol{\psi}, \quad \nabla \cdot \boldsymbol{\psi} = 0. \tag{2.23}$$

To work out the decomposition we only need to solve a Poisson equation

$$\nabla^2\phi = \vartheta \quad \text{in } V_f; \quad \frac{\partial\phi}{\partial n} = \boldsymbol{n} \cdot \boldsymbol{u} \quad \text{at } \partial V_f. \tag{2.24a,b}$$

Then, $\nabla \times \boldsymbol{\psi} = \boldsymbol{u} - \nabla\phi$ and the local time derivative of velocity can be written as

$$\boldsymbol{u}_{,t} = \nabla\phi_{,t} + \nabla \times \boldsymbol{\psi}_{,t}. \tag{2.25}$$

Therefore, substituting (2.22) into (2.9*a*) yields

$$\boldsymbol{F} = \boldsymbol{F}_L + \boldsymbol{F}_T + \boldsymbol{F}_B, \tag{2.26}$$

where subscripts L and T stand for longitudinal and transverse, respectively. In advection form, their expressions are:

$$\boldsymbol{F}_L = -\int_{V_f} \rho \boldsymbol{j}_L \mathrm{d}V - \frac{1}{n-1}\int_{\partial V_f} \boldsymbol{x} \times (\boldsymbol{n} \times \rho \boldsymbol{j}_L)\mathrm{d}S, \tag{2.27a}$$

$$\boldsymbol{F}_T = -\int_{V_f} \rho \boldsymbol{j}_T \mathrm{d}V - \frac{1}{n-1}\int_{\partial V_f} \boldsymbol{x} \times (\boldsymbol{n} \times \rho \boldsymbol{j}_T)\mathrm{d}S + \boldsymbol{F}_\Sigma, \tag{2.27b}$$

where

$$\boldsymbol{j}_L = \alpha\nabla\phi_{,t} + \beta R\nabla(\alpha T) - \beta\nu_\theta\nabla\vartheta, \tag{2.28a}$$

$$\boldsymbol{j}_T = \alpha\nabla \times \boldsymbol{\psi}_{,t} + \alpha\boldsymbol{\omega} \times \boldsymbol{u} + \beta\nu\nabla \times \boldsymbol{\omega}. \tag{2.28b}$$

https://doi.org/10.1017/jfm.2014.403 Published online by Cambridge University Press

Remarks. (i) The transverse force (T-force) $\boldsymbol{F}_T$ is reduced to the incompressible vortex force as $M \to 0$. As explained above and indicated by (2.21), the extra compressible portion with factor $\beta(M)$ in both $\boldsymbol{F}_T$ and $\boldsymbol{F}_L$ comes from the need to balance the gradient of thermodynamic pressure. Factor $\alpha(M)$ represents a modulation of the existing shearing process by compressibility (Mao *et al.* 2011). Of course, the variable density also has an (implicit here) M-dependent modulation of shearing.

(ii) Equation (2.19*b*) shows that the longitudinal force (L-force) $\boldsymbol{F}_L$ results from a competition between total enthalpy h_0 and internal energy e, the gradients of which are often in opposite directions. This competition is now reflected by factor $\alpha(M)$ inside the gradient operator.

(iii) At large Re, as long as Σ is not very close to the body surface, $\boldsymbol{F}_\Sigma$ can be neglected. If we only consider steady translational motion of a rigid body, then $\boldsymbol{F}_B$ is also absent.

3. Numerical example: compressible flow over a circular cylinder

3.1. *Force formulae adopted*

To demonstrate the preceding LT-force theory, we conducted a numerical computation of a two-dimensional uniform flow at infinity over a stationary circular cylinder with unit radius. We set the origin of $\boldsymbol{x}$ at the centre of the cylinder and choose the outer boundary Σ of the analysis domain as concentric circles of radii $R \geqslant 1$, in which our formulae will be applied. In polar coordinates (r, θ) with the x-axis in the direction of $\theta = 0$, by (2.9*a*) and (1.4*a*) where the two viscous terms can be cast as the normal and tangential components of $\mu\boldsymbol{\nabla}\omega$, the drag of the cylinder in the advection form has one field integral and two boundary integrals:

$$D = D_{V,j} + D_{\Sigma,j} + D_{\Sigma,vis}, \tag{3.1}$$

where

$$D_{V,j} = -\int_{V_f} \rho j_x \mathrm{d}S, \tag{3.2a}$$

$$D_{\Sigma,j} = R^2 \oint_\Sigma \rho j_\theta \sin\theta \mathrm{d}\theta, \tag{3.2b}$$

$$D_{\Sigma,vis} = \mu R^2 \oint_\Sigma \left(\frac{\partial \omega}{\partial r} \sin\theta - \frac{1}{R}\frac{\partial \omega}{\partial \theta}\cos\theta \right) \mathrm{d}\theta. \tag{3.2c}$$

The drag coefficient is defined by

$$C_d \equiv \frac{D}{\rho_\infty U_\infty^2 R_0}, \tag{3.3}$$

where D is the drag of the circular cylinder per unit length, and $R_0 = 1.0$ is the radius of the cylinder. For comparison, the standard formula (2.2) will also be used to calculate the drag coefficient, which will be denoted as 'standard'. Furthermore, the normalized drag coefficient is defined by

$$(C_d)^* \equiv \frac{C_d}{\text{standard}}, \tag{3.4}$$

https://doi.org/10.1017/jfm.2014.403 Published online by Cambridge University Press

and the non-normalized and normalized time-averaged drag coefficients will be denoted by $\overline{C}_d$ and $(\overline{C}_d)^*$, respectively.

From (2.27*a*) and (2.27*b*), we have

$$D_L = D_{V,j_L} + D_{\Sigma,j_L}, \tag{3.5a}$$

$$D_T = D_{V,j_T} + D_{\Sigma,j_T} + D_{\Sigma,vis}. \tag{3.5b}$$

The corresponding drag coefficients are denoted as $C_{d,L}$, $C_{d,T}$, and so on.

3.2. *Numerical method and validation*

Our computation used an O-grid with polar variables (r, θ) that are transformed to discrete variables (i, j). Here, i is simply scaled from polar angle θ by $\theta = 2\pi i/m$, $i = 0, 1, \ldots, m$; j denotes the radial variable and takes integer values $j = 0, 1, \ldots, n$. Let $r = Z$ denote the outer boundary of the computational domain; r and j are related by

$$\frac{r-1}{Z-1} = 1 - \delta\frac{K-1}{K+1}, \quad \text{with } K(j) = \left(\frac{\delta+1}{\delta-1}\right)^{1-j/n}, \tag{3.6}$$

where $\delta > 1$ is a parameter, which implies a dense grid distribution near the solid boundary when δ is close to 1 (see Chang & Lei 1996).

In the present study, we have a grid system $m \times n = 512 \times 512$, $Z = 200$, and $\delta = 1.0001$. The free-stream Mach number M_∞ is from 0.2 to 2.0 with interval 0.1, and the Reynolds number $Re = \rho_\infty U_\infty R_0/\mu$ is always 1000. The initial condition is set as the free-stream quantities. The pressure far-field boundary condition is used on the outer boundary. No-slip and adiabatic conditions are applied on the cylinder surface.

The OpenCFD-EC2D-1.5.4 program developed by Professor X. L. Li of the Chinese Academy of Sciences is employed to solve the compressible Navier–Stokes equations. In this open-source software, the governing equations are numerically solved by a finite-volume method, the convective terms are discretized by a third-order WENO scheme for shock capturing, and the viscous terms by a second-order central difference. For temporal terms a second-order LU-SGS method is used with dimensionless time step $\Delta t = 1.0 \times 10^{-3}$. The dynamic viscosities are assumed to be constant, and no turbulence model is used.

To validate the method, convergence checks have been carried out to assess the effect of grid number and domain size. We found that the case of $M_\infty = 0.8$ is most sensitive to grid number and computational domain size Z. For this case we calculated the drag coefficients by standard formula (2.2) with different grid systems and Z but with the same first normal grid spacing. The corresponding time-averaged drag coefficients are shown in figure 1. As grid number or Z increases, the convergence trend is obvious, indicating that the computed results are independent of the grid number and computational domain size. The results given below have been calculated on the finest grid and the largest domain.

3.3. *Choice of the location of the outer boundary of the analysis domain*

While the computational domain is fixed as defined above, the location of the outer boundary Σ of radius R of the analysis domain is allowed to vary arbitrarily in principle. But in practical computation the choice of R needs to be optimized. To see this, the normalized contributions of time-averaged drag coefficients, $(\overline{C}_d)^*$, $(\overline{C}_{d,L})^*$, $(\overline{C}_{d,T})^*$, and $(\overline{C}_{d,\Sigma_{vis}})^*$, with varying R for $M_\infty = 0.2$, 0.8, 0.9, 2.0 are shown in

https://doi.org/10.1017/jfm.2014.403 Published online by Cambridge University Press

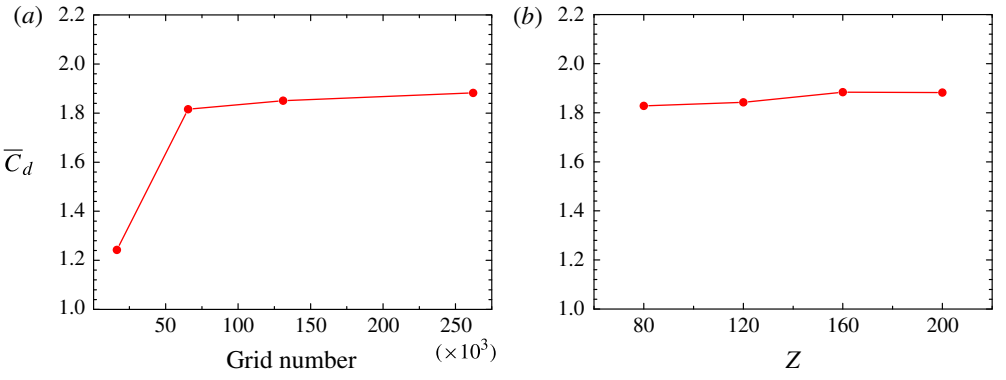


FIGURE 1. (Colour online) The time-averaged drag coefficient $\overline{C}_d$ for $M_\infty = 0.8$ computed with (*a*) different grid numbers and (*b*) different computational domain sizes, Z.

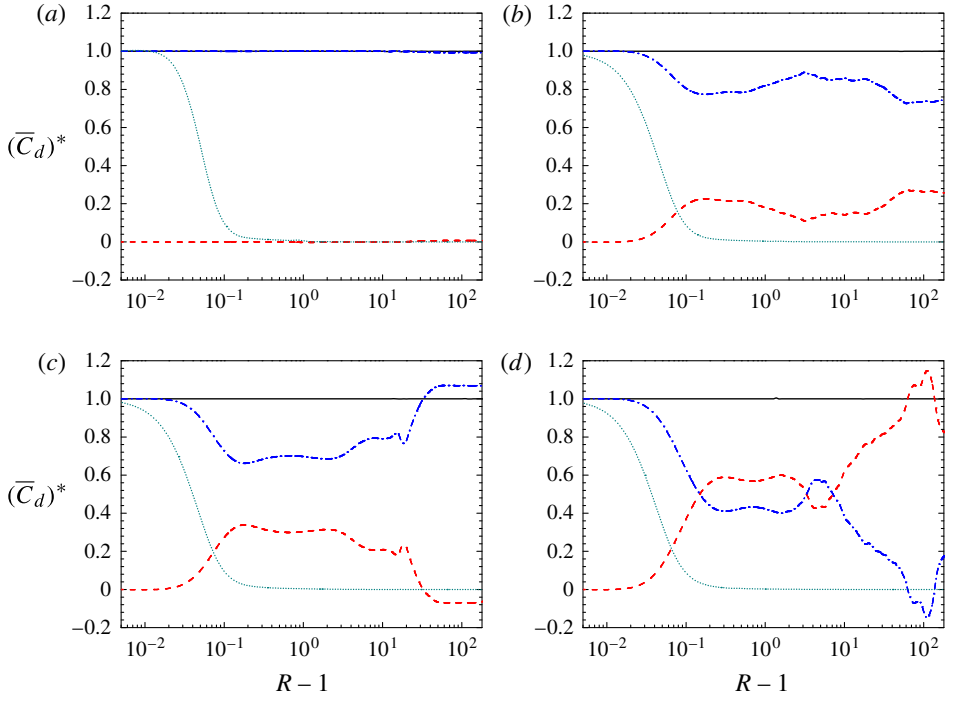


FIGURE 2. (Colour online) Normalized contributions of drag coefficients by varying boundary position Σ of radius R. Solid line, $(\overline{C}_d)^*$; dashed line, $(\overline{C}_{d,L})^*$; dashed-dotted line, $(\overline{C}_{d,T})^*$; dotted line, $(\overline{C}_{d,\Sigma_{vis}})^*$. (*a*) $M_\infty = 0.2$. (*b*) $M_\infty = 0.8$. (*c*) $M_\infty = 0.9$. (*d*) $M_\infty = 2.0$.

figure 2. (In our numerical examples we found that the unsteady part of the L-force is negligibly small and the flow unsteadiness is mainly caused by vortex shedding, thus we just add the whole explicit unsteady part of the total force to the T-force to simplify the analysis.) In all cases $(\overline{C}_d)^* \equiv 1$, which confirms the independence of the analysis-domain size from the computed forces. In this figure, a logarithmic scale is

https://doi.org/10.1017/jfm.2014.403 Published online by Cambridge University Press

used to highlight the middle field so that the effect of R can be seen more clearly. Then we observe the following.

First, the term $(\overline{C}_{d,\Sigma_{vis}})^*$ shows similar behaviour at different Mach numbers. When $R-1$ is close to zero (near-wall region), this term contributes almost all of the drag, consistent with the boundary form of the force that may follow from setting $V_f = 0$ in (2.8) such that $\boldsymbol{F} = \boldsymbol{F}_\Sigma + \boldsymbol{F}_B$, see Wu *et al.* (2006, p. 620). But when $R-1$ is of $O(1)$ (middle region) or larger (far region), it decays to zero quickly.

Secondly, in the middle region the transverse force provides almost all of the drag at low Mach numbers, while at higher Mach numbers both the L-force and T-force are significant. The division of the L-force and T-force becomes R-independent if R is large enough, since then all flow structures are in the diagnosis domain and surface integrals are zero.

Thirdly, since our formulae are not yet applicable to non-smooth solutions, the trends of the L-force and T-force in figure 2(*c*,*d*) for large values of R may not be reliable when the domain boundary intersects shocks.

Fortunately, in our cases strong shock waves do not appear for $R \leqslant 2$, so we choose $R = 2$ in our following analysis.

3.4. *Flow structures*

In the LT-force formula the typical local flow structures associated with nonlinear transverse and longitudinal processes are characterized by vector fields $-\rho\alpha(\boldsymbol{\omega} \times \boldsymbol{u})$ and $-\rho\beta R\nabla(\alpha T)$, respectively. The instantaneous x-components of these vector fields, responsible for the drag, are shown respectively in figures 3 and 4 for $M_\infty = 0.2, 0.8, 0.9, 2.0$. The dashed-dotted line circle is our diagnosis boundary Σ.

Figure 3 shows that there exists a strong boundary layer along the front wall of the circular cylinder, and the flow separates at about the shoulder of the cylinder, forming a strong free shear layer. But whether the latter develops into shedding vortices depends on the Mach number. The familiar Kármán vortex street occurs typically at lower M_∞, see figure 3(*a*,*b*). Figure 3(*c*,*d*) show that the vortex shedding is suppressed at higher M_∞, where the flow transforms from unsteady to quasi-steady. Therefore, in the studied range of M_∞ there are only two basic flow patterns for $\rho\alpha\omega v$, and their switching occurs at a critical $M_\infty = M_{cr} \approx 0.9$.

The vortex shedding also leaves footprints in figure 4(*a*,*b*) due to the lower pressure at centres of vortices. At very small Mach number, the compressing effect is negligible, see figure 4(*a*). As M_∞ increases to 0.6, a small supersonic flow zone appears at the shoulder of the body. As a result, the compressibility effect begins to be significant. As M_∞ becomes larger, shock waves appear behind the cylinder, which interact with the shedding vortices that make the flow more oscillatory. The shock waves and shock–vortex interaction are clearly seen from figure 4(*b*).

The unsteady shock-wave interaction is enhanced as M_∞ increases up to $M_{cr} \approx 0.9$, at which the vortex shedding begins to be suppressed, the shock–vortex interaction disappears, and the flow becomes quasi-steady (figure 4*c*). This phenomenon has also be found by Xu, Chen & Lu (2009) at a much larger Reynolds number, $Re = 2 \times 10^5$.

Then, figure 4(*d*) exhibits a detached bow shock ahead of the body. Upstream of the separated shear layers there exist a pair of strong expansion fans, which are reflected and re-compressed to form a trailing shock wave.

4. Preliminary flow diagnosis

4.1. *Drag constituents*

How local flow structures from transverse and longitudinal processes identified above affect the LT-force can be seen from figure 5, which displays the variation of time-

https://doi.org/10.1017/jfm.2014.403 Published online by Cambridge University Press

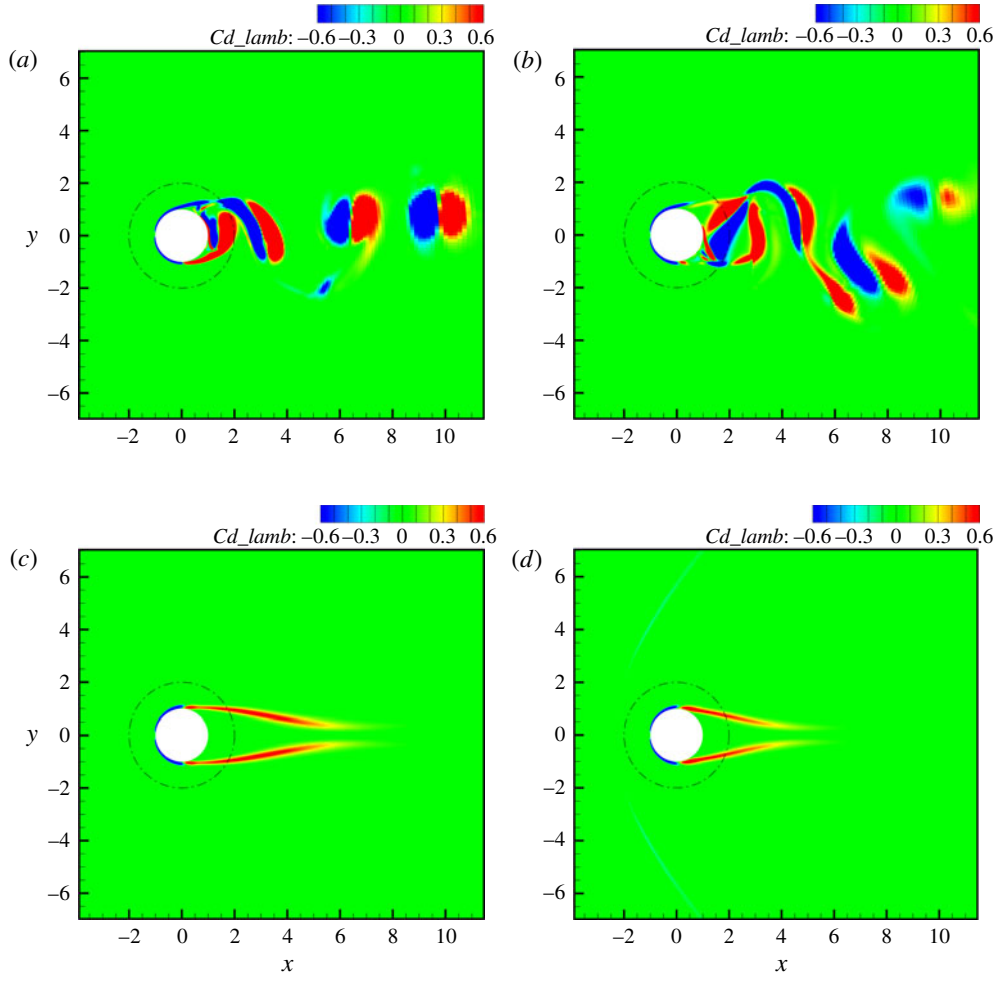


FIGURE 3. Instantaneous field distributions of the volume integrand, where *Cd_lamb* denotes $\rho\alpha\omega v$, from -0.6 to 0.6. (*a*) $Cd_lamb \in [-21.0, 13.6]$; $M_\infty = 0.2$. (*b*) $Cd_lamb \in [-9.2, 4.5]$; $M_\infty = 0.8$. (*c*) $Cd_lamb \in [-8.0, 0.9]$; $M_\infty = 0.9$. (*d*) $Cd_lamb \in [-6.6, 0.8]$; $M_\infty = 2.0$.

averaged drag coefficients $\overline{C}_d$ and its constituents with free-stream Mach number M_∞. The results are calculated by (2.2), (3.1), (3.5*a*) and (3.5*b*), which are denoted as 'standard', $\overline{C}_d$, $\overline{C}_{d,T}$ and $\overline{C}_{d,L}$, respectively.

On the one hand, $\overline{C}_{d,L}$ is negligibly small at $M_\infty \leqslant 0.6$, and it increases quickly from 0.07 to 0.57 as M_∞ varies from 0.6 to 0.9. Then it decreases slightly from $M_\infty = 0.9$ to 1.1, after which it increases almost linearly with M_∞. The initial quick growth of $\overline{C}_{d,L}$ is simply due to the increasing effect of compressibility as M_∞ increases, and the small plateau and final linear growth are due to the spatial–temporal average effect of local Mach number. These effects will be seen more directly in § 5.2.

On the other hand, $\overline{C}_{d,T}$ varies in a more complicated manner with M_∞, due to the shedding of vortices as well as their interaction with shock waves. At first, it increases from 1.65 to 1.81 as M_∞ goes from 0.2 to 0.4, simply due to the modulation of the

https://doi.org/10.1017/jfm.2014.403 Published online by Cambridge University Press

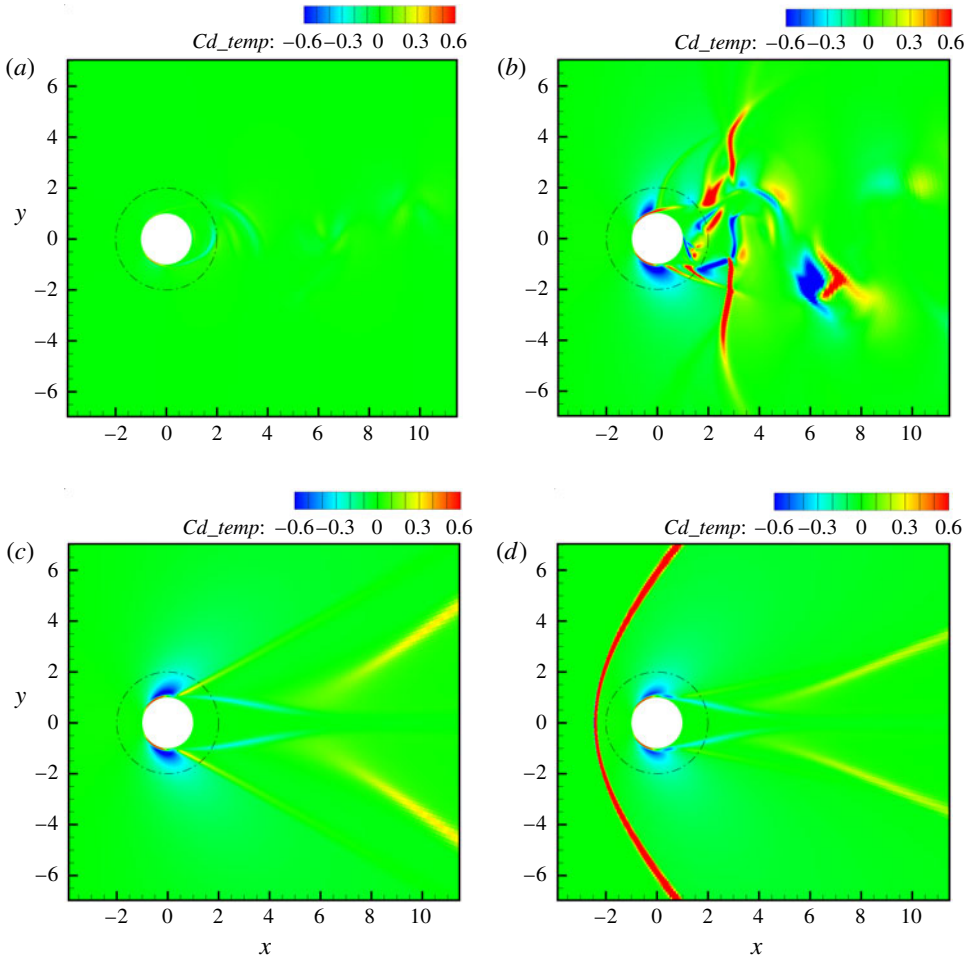


FIGURE 4. Instantaneous field distributions of the volume integrand, where *Cd_temp* denotes $-\rho\beta R(\alpha T)_{,x}$, from -0.6 to 0.6. (*a*) $Cd_temp \in [-0.25, 0.55]$; $M_\infty = 0.2$. (*b*) $Cd_temp \in [-1.5, 9.8]$; $M_\infty = 0.8$. (*c*) $Cd_temp \in [-0.7, 1.3]$; $M_\infty = 0.9$. (*d*) $Cd_temp \in [-1.1, 11.5]$; $M_\infty = 2.0$.

compressing progress. As M_∞ increases from 0.5 to 0.9, local shock waves appear, which interact with shedding vortices and make the T-drag decrease from 1.72 to 1.30. Then for $M_\infty \geqslant 0.9$, the vortex shedding is suppressed and the flow becomes quasi-steady, and $\overline{C}_{d,T}$ decreases also almost linearly with M_∞.

Finally, the calculated LT-force (the sum of the L-force and T-force), $\overline{C}_d$, agrees perfectly with the result of the standard force formula, indicating the correctness of the LT-force theory.

4.2. *Modulation of the T-force by the compressing process*

As shown by figure 5, the T-force changes more irregularly with M_∞ than the L-force, due to the highly nonlinear evolution of vortical structures and their sensitivity to M_∞. Inside the flow, the complexity of the T-force comes mainly from the nonlinearity of the Lamb vector, which is at the crossroad of shearing and compressing.

https://doi.org/10.1017/jfm.2014.403 Published online by Cambridge University Press

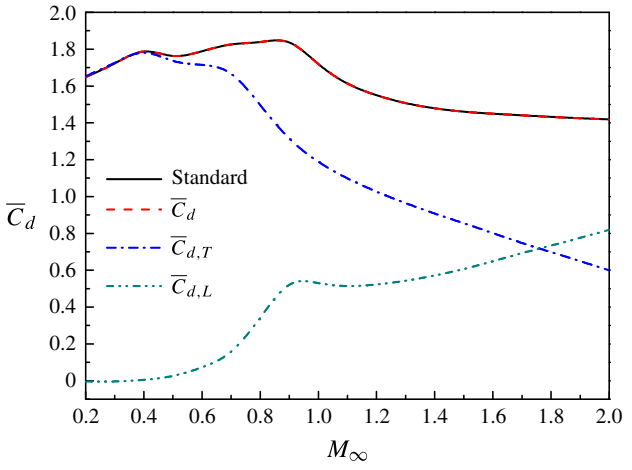


FIGURE 5. (Colour online) Mach dependence of the time-averaged drag coefficients and its components calculated by (2.2), (3.1), (3.5*a*) and (3.5*b*).

From (2.23) the Lamb vector can be written as

$$\boldsymbol{\omega}\times\boldsymbol{u}=\boldsymbol{\omega}\times\boldsymbol{U}+\boldsymbol{\omega}\times\nabla\varphi+\boldsymbol{\omega}\times(\nabla\times\boldsymbol{\psi}), \tag{4.1}$$

where

$$\phi=\varphi+\boldsymbol{U}\cdot\boldsymbol{x};\quad \nabla^2\varphi=\vartheta,\quad \nabla^2\boldsymbol{\psi}=-\boldsymbol{\omega}. \tag{4.2a–c}$$

Then the Lamb vector itself contains self-linearity ($\boldsymbol{\omega}\times\boldsymbol{U}$, SL for short) and self-nonlinearity ($\boldsymbol{\omega}\times(\nabla\times\boldsymbol{\psi})$, SN for short) of the shearing process, and cross-modulation ($\boldsymbol{\omega}\times\nabla\varphi$, CM for short) between shearing and compression (Mao *et al.* 2011). Note that the SL component makes no contribution to drag. The M_∞-dependence of the part of time-averaged drag coefficients from the Lamb vector and its SN and CM components is shown in figure 6.

In low subsonic flow, the SN-drag increases with M_∞. When the flow has supersonic regions it starts to drop and becomes negative and reaches a minimum at about M_{cr}. Above that it increases with M_∞ again but remains negative. The major change in the trend of SN-drag is caused by the transition of the wake flow pattern from a highly unsteady Kármán vortex street (self-nonlinearity) to its suppression by compressibility and shock waves, which even turns the pure shearing vortex force into a thrust at $M_\infty\approx 0.7$.

In contrast, the CM-drag is increasingly dominant with a simpler variation, which keeps the full Lamb vector as a source of drag. It increases with M_∞ until M_{cr} where the flow becomes quasi-steady and the vortex shedding is suppressed. As a result, it begins to decrease with M_∞.

4.3. *Boundary vorticity flux (BVF) and boundary vorticity*

It is known that the boundary form of the force formula, in terms of the moment of BVF, may further reveal the origin of near-wall vortical structures. In our case BVF depends only on the gradient of the normal stress Π, denoted by σ:

$$\sigma\equiv-\nu\frac{\partial\omega}{\partial r}=-\frac{1}{\rho R_0}\frac{\partial\Pi}{\partial\theta}\quad\text{at } r=R_0, \tag{4.3}$$

https://doi.org/10.1017/jfm.2014.403 Published online by Cambridge University Press

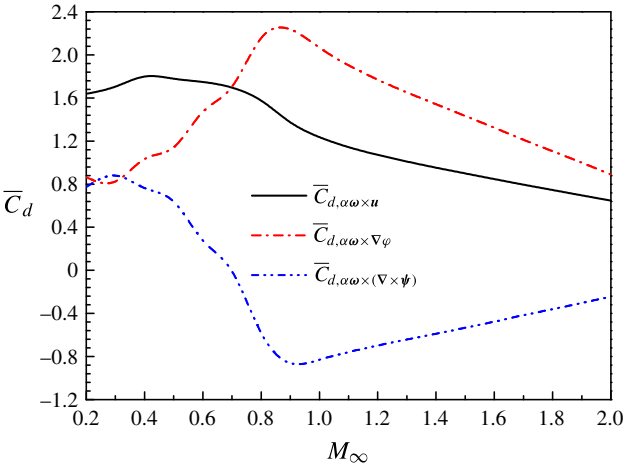


FIGURE 6. (Colour online) Mach dependence of the time-averaged drag coefficients constituted by the Lamb vector part and its components.

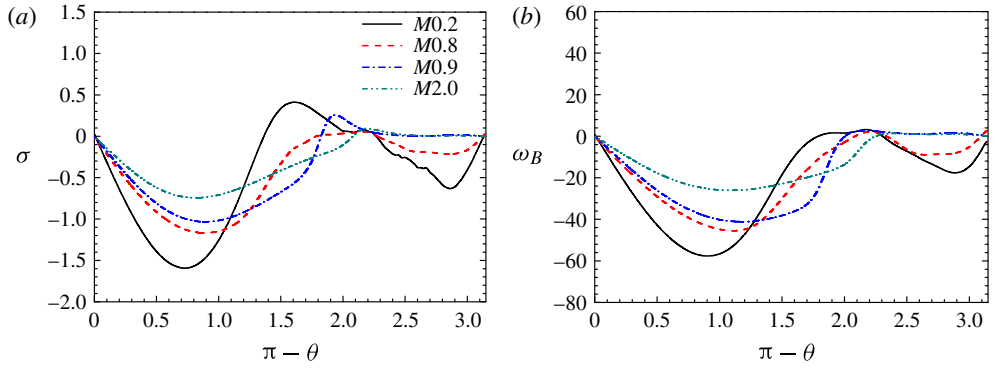


FIGURE 7. (Colour online) The time-averaged distribution of (*a*) boundary vorticity flux and (*b*) boundary vorticity, on the upper surface of a circular cylinder, for various M_∞ values.

which measures the boundary coupling between shearing and compressing processes. The time-averaged distributions of σ at typical M_∞ are shown in figure 7(*a*). The magnitude of the peak value of BVF decreases monotonically as M_∞ varies. Meanwhile, as M_∞ increases, the location of the peak value of σ moves downstream, consistent with the fact that in subsonic compressible flow the lateral development of the flow becomes wider than incompressible flow, and hence the pressure gradient is milder. In particular, the adverse gradient of Π at the lee side of the cylinder occurs further downstream and is weakened at larger M_∞; thus the boundary-layer separation is somewhat delayed (figure 3). But once a shock appears on the wall, BVF changes sign abruptly to promote separation (figure 4*c*).

The boundary vorticity (BV) is responsible for the friction force:

$$\boldsymbol{F}_{fric} = \int_{\partial B} \mu \boldsymbol{n} \times \boldsymbol{\omega} \mathrm{d}S. \tag{4.4}$$

https://doi.org/10.1017/jfm.2014.403 Published online by Cambridge University Press

The time-averaged ω_B distribution for typical Mach numbers is shown in figure 7(*b*). Like BVF, the magnitude of the peak value of ω_B decreases monotonically as M_∞ increases. As a space–time effect of BVF accumulated on the wall (Wu *et al.* 2006), BV always changes its sign only after (along the local stream direction) the BVF does. This is seen clearly in figure 7.

5. Mach-number dependence of drag constituents and the possibility of seeking similarity rules

The appearance of two local Mach-number factors $\alpha(M)$ and $\beta(M)$ is a remarkable feature of the LT-force formulae. For the T-force $\alpha(M)$ exists for incompressible flow and is modulated by longitudinal processes at $M > 0$, while for the L-force $\beta(M)$ appears only when $M > 0$. Unlike other quantities in the formulae, these factors are independent of any specific flow fields but derived solely from the governing equations, and hence are universal.

In the past, the appearance of universal Mach-number factors always implied certain similarity rules that can greatly facilitate relevant aerodynamic analyses, experiments and designs. The simplest case is seen in classic linearized high-speed aerodynamics where the flow over a thin or slender streamlined body is assumed inviscid, irrotational, and steady without entropy increase. It has only a single linear compressing process governed by the disturbance velocity-potential equation

$$(1 - M_\infty^2)\phi_{xx} + \phi_{yy} + \phi_{zz} = 0. \tag{5.1}$$

Here, the single Mach-number factor $\sqrt{1 - M_\infty^2}$ is the basis of the well-known Prandtl–Glauert and Goethert similarity rules. More complicated than this are the von Kármán transonic similarity rule, the Kármán–Tsien high-subsonic similarity rule, and Tsien's hypersonic similarity rule, etc., all based on a single decoupled longitudinal process. It is therefore highly desirable to explore the implications of $\alpha(M)$ and $\beta(M)$ for the present complex and multi-process flow, to seek the possibility of finding new approximate similarity rules and, if such rules are violated, to explain why. In this section we make a preliminary observation and discussion.

5.1. *M-factors and transverse-force constituents in cylinder flow*

Figure 8 displays the Mach-number dependence of the time-averaged drag coefficient from the T-force, $\overline{C}_{d,T}$, and its major constituent from the Lamb vector, $\alpha(M)\boldsymbol{\omega} \times \boldsymbol{u}$. Two universal Mach-number factors $\alpha(M_\infty)$ and $\beta(M_\infty)$ are also plotted in figure 8. Here and below, we assume that the value of M_∞ is an acceptable approximation of the spatial–temporal average of local $M(\boldsymbol{x}, t)$ over the entire flow field (except in supersonic flow), which is indeed so at least for high-subsonic thin-airfoil attached flow (see von Kármán 1941).

We first observe that the T-force comes almost solely from the $\alpha(M)$-weighted Lamb-vector term, i.e. $\overline{C}_{d,\alpha\boldsymbol{\omega}\times\boldsymbol{u}}$. Its difference from the full $\overline{C}_{d,T}$ comes from the contribution of $\alpha\boldsymbol{u}_{,t}$ and $\beta\nu\boldsymbol{\nabla}\times\boldsymbol{\omega}$, which can be neglected in our following discussion. Then, the single curve $1.6\alpha(M_\infty)$ fits $\overline{C}_{d,\alpha\boldsymbol{\omega}\times\boldsymbol{u}}$ only over a very small low-M_∞ regime. The same happens if $\alpha(M_\infty)$ is replaced by $\sqrt{1 - M_\infty^2}$ as in the Prandtl–Glauert similarity rule and by the Kármán–Tsien nonlinear similarity M_∞-factor (curves not shown). According to the discussion given in § 4.2, the increase of $\overline{C}_{d,\alpha\boldsymbol{\omega}\times\boldsymbol{u}}$ at $M_\infty \approx 0.2$ and its decrease again at $M_\infty \approx 0.4$ should be mainly attributed to

https://doi.org/10.1017/jfm.2014.403 Published online by Cambridge University Press

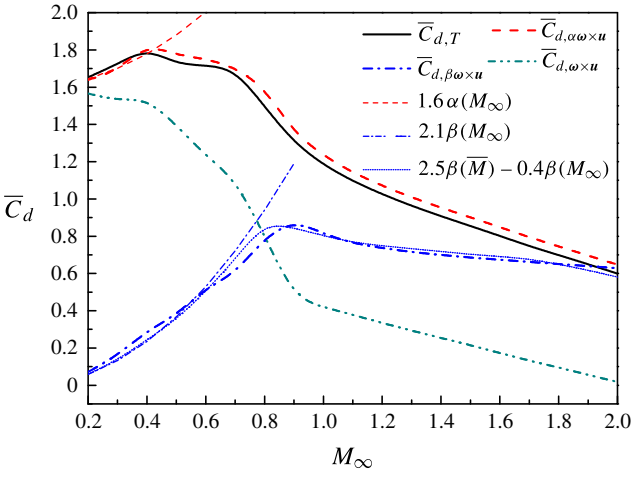


FIGURE 8. (Colour online) Mach dependence of the time-averaged constituents of drag coefficient from the T-force and Lamb vector, together with three fitting curves.

the time-averaged effect of the highly localized Lamb-vector field in the boundary layer and wake vortices modulated by local compressing structures, although in this M_∞-range the direct contribution of $\overline{C}_{d,L}$ is still negligible.

The $\alpha(M)$-weighted Lamb vector can, however, be further split into the 'bare' Lamb vector $\boldsymbol{\omega}\times\boldsymbol{u}$ and $\beta(M)\boldsymbol{\omega}\times\boldsymbol{u}$ which represents the modulation of the T-force by $-k\boldsymbol{\nabla}\ln\rho$, which are also shown in figure 8. Remarkably, the M-dependence of the latter is much smoother and simpler than the former, so that the single curve $2.1\beta(M_\infty)$ fits $\overline{C}_{d,\beta\boldsymbol{\omega}\times\boldsymbol{u}}$ very well up to $M_\infty\approx 0.6$. This is in sharp contrast to the case of 1.6α, indicating that although the strong Kármán vortex street does not have a universal Mach-number dependence, the way in which the vortex street is modulated by $-k\boldsymbol{\nabla}\ln\rho$ still does.

Note that this universal M-dependence of $\beta(M)\boldsymbol{\omega}\times\boldsymbol{u}$ would not be found if we had used (2.15) without moving onto (2.22) by further decomposing $-k\boldsymbol{\nabla}\ln\rho$ into several dynamic constituents. But so far we have not found a good fitting curve of $\beta\boldsymbol{\omega}\times\boldsymbol{u}$ for the supersonic regime with a single M_∞-factor. In fact, unlike inviscid and attached flow over a thin wing at small angles of attack where a single M_∞ suffices for constructing a similarity rule, for the present separated flow over a bluff body one needs at least two constant Mach numbers. In addition to M_∞, an averaged Mach number for the disturbance flow should also be considered. While it could be possible to rationally derive the optimal use of these two Mach numbers (which is under investigation), as a preliminary search of new similarity rules we shall be satisfied below with their linear combinations with coefficients determined by numerical fitting. Then we use a fitting curve with a combination of M_∞ and temporal–spatial average of local Mach number $\overline{M}$ over the diagnosis domain. The result is also shown in figure 8, which fits the whole flow regime very well.

5.2. *M-factors and longitudinal-force constituents in cylinder flow*

The Mach-number dependence of the L-force comes almost entirely from the density-gradient term $-k\boldsymbol{\nabla}\ln\rho$. Thus, in figure 9 we plot the computed time-averaged drag coefficient from the integral of this term, $\overline{C}_{d,-k\boldsymbol{\nabla}\ln\rho}$, along with its constituents over

https://doi.org/10.1017/jfm.2014.403 Published online by Cambridge University Press

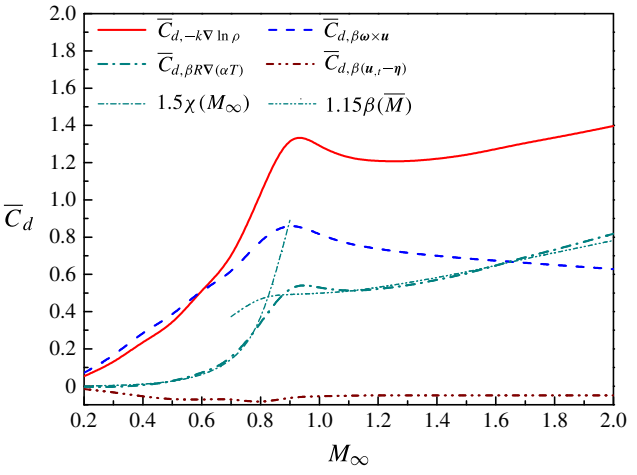


FIGURE 9. (Colour online) Mach dependence of the time-averaged drag coefficients constituted by $-k\nabla\ln\rho$ integral and its component integrals, together with two fiting curves.

different M_∞. The figure shows that the L-drag due to $-k\nabla\ln\rho$ consists mainly of that due to $\beta\boldsymbol{\omega}\times\boldsymbol{u}$ (the 'Lamb-part'), that we have just discussed and $\beta R\nabla(\alpha T)$ (the 'temp-part'). The latter dominates the L-drag. Once again, the drag from the flow unsteadiness term and viscous term, $\beta(\boldsymbol{u}_{,t}-\boldsymbol{\eta})$, is negligibly small in a large range of the Mach number.

Evidently, compared with the T-drag from $\boldsymbol{\omega}\times\boldsymbol{u}$, the curve $\overline{C}_{d,-k\nabla\ln\rho}$ has much smoother variation with M_∞. It increases rapidly till M_{cr}, then decreases mildly to reach a minimum at $M_\infty\approx 1.2$, and then increases again. This smooth variation suggests a better chance of finding universal fitting curves. We have seen that this is indeed true for the 'Lamb-part', and now let us focus on the 'temp-part'. However, owing to the involvement of $\nabla\alpha=\nabla(1+\beta)$ therein, the fitting cannot be simply made using $\beta(M_\infty)$ or $\alpha(M_\infty)\beta(M_\infty)$. Instead, we have to re-express $\beta R\nabla(\alpha T)$ more carefully.

First, by (2.19*b*) we have

$$\frac{T_0}{T}=1+\frac{\gamma-1}{2}M^2, \tag{5.2}$$

so the 'temp-part' can be rewritten as

$$\beta R\nabla(\alpha T)=\beta c_p T_0\frac{\nabla T_0}{T_0}-\frac{\beta c_v T_0}{1+\dfrac{\gamma-1}{2}M^2}\frac{\nabla T}{T}. \tag{5.3}$$

Also, letting $q=|\boldsymbol{u}|$, from the equations of energy, entropy and state, we have

$$(\gamma-1)M^2\frac{\nabla q}{q}+\frac{\nabla T}{T}=\left(1+\frac{\gamma-1}{2}M^2\right)\frac{\nabla T_0}{T_0}, \tag{5.4a}$$

$$\frac{\nabla p}{p}-\gamma\frac{\nabla\rho}{\rho}=\frac{\nabla s}{c_v}, \tag{5.4b}$$

$$\frac{\nabla p}{p}-\frac{\nabla\rho}{\rho}=\frac{\nabla T}{T}. \tag{5.4c}$$

https://doi.org/10.1017/jfm.2014.403 Published online by Cambridge University Press

Here, (5.4*a*) can be re-expressed as

$$\frac{\boldsymbol{\nabla} q}{q} = \frac{1+\dfrac{\gamma-1}{2}M^2}{(\gamma-1)M^2}\frac{\boldsymbol{\nabla} T_0}{T_0} - \frac{1}{(\gamma-1)M^2}\frac{\boldsymbol{\nabla} T}{T}, \tag{5.5}$$

while combining (5.4*b*) and (5.4*c*) yields

$$\frac{\boldsymbol{\nabla}\rho}{\rho} = \frac{1}{\gamma-1}\frac{\boldsymbol{\nabla} T}{T} - \frac{\boldsymbol{\nabla} s}{R}. \tag{5.6}$$

To proceed, we assume that the flow is steady since the effect of flow unsteadiness on $\overline{C}_d$ has been found negligible. In order to find universal Mach-number factors, we consider a sufficiently thin fluid tube with varying sectional area A, so that

$$\frac{\mathrm{d}\rho}{\rho} + \frac{\mathrm{d}q}{q} + \frac{\mathrm{d}A}{A} = 0. \tag{5.7}$$

Then by substituting (5.5) and (5.6) into (5.7) we obtain

$$\frac{\mathrm{d}T}{T} = \frac{1+\dfrac{\gamma-1}{2}M^2}{1-M^2}\frac{\mathrm{d}T_0}{T_0} - \frac{(\gamma-1)M^2}{1-M^2}\left(\frac{\mathrm{d}s}{R} - \frac{\mathrm{d}A}{A}\right), \tag{5.8}$$

substitution of which into (5.3) finally leads to

$$\beta R d(\alpha T) = \chi(M) h_0 \left(\frac{\mathrm{d}s}{R} - \frac{\mathrm{d}A}{A}\right) + \zeta(M)\mathrm{d}h_0, \tag{5.9}$$

where we have defined a new pair of local Mach-number factors

$$\chi(M) = \frac{(\gamma-1)M^4}{[2+(\gamma-1)M^2](1-M^2)}, \tag{5.10a}$$

$$\zeta(M) = \frac{[(\gamma-1)-\gamma M^2]M^2}{2(1-M^2)}, \tag{5.10b}$$

with

$$|\chi(1)| = \infty, \quad |\zeta(1)| = \infty, \quad |\chi(\infty)| = 1, \quad \zeta(\infty) = \frac{\gamma}{2}M^2. \tag{5.11a–d}$$

While χ takes care of the M-dependence of the longitudinal processes for constant h_0, ζ takes care of that for varying h_0. The latter occurs mainly in supersonic flow associated with strong heat flux; but compared to the first term of (5.9) it should still be relatively small except for very large M. We thus leave it aside.

For subsonic flows, we may just take $\chi(M_\infty)$ as the mean value of $\chi(M)$ as we did before for $\alpha(M)$ and $\beta(M)$. Then (2.27*a*) can be written as

$$\boldsymbol{F}_L \approx \chi(M_\infty) f_1(\mathrm{d}A/A, \boldsymbol{\nabla} s) + \zeta(M_\infty) f_2(\boldsymbol{\nabla} h_0), \tag{5.12}$$

where f_1 and f_2 are some unknown functions. Since in subsonic flows the variations of entropy and total enthalpy are very small, we speculate that

$$C_{d,\beta R\nabla(\alpha T)} \approx \chi(M_\infty) f_1(\mathrm{d}A/A) \quad (M_\infty < 1). \tag{5.13}$$

https://doi.org/10.1017/jfm.2014.403 Published online by Cambridge University Press

If we take $f_1 \approx 1.5$, we obtain the left-hand fitting curve in figure 9. It fits $\overline{C}_{d,\beta R\nabla(\alpha T)}$ perfectly until $M_\infty \approx 0.8$.

For supersonic flows, once again M_∞ should no longer be an acceptable approximation value of the spatial–temporal average of local $M(\boldsymbol{x}, t)$ over the entire diagnosis flow field. Thus we turn to $\overline{M}$ again. At the same time, it is known that for one-dimensional normal shock waves, αT varies very smoothly before and after shock waves at moderate Mach numbers. We thus speculate that

$$C_{d,\beta R\nabla(\alpha T)} \approx \beta(\overline{M}) f_3. \tag{5.14}$$

If we take $f_3 = 1.15$, we obtain the right-hand fitting curve in figure 9. It fits $\overline{C}_{d,\beta R\nabla(\alpha T)}$ well when $M_\infty \gtrsim 1.0$.

5.3. *Discussion*

The Mach-number factors $\alpha(M)$, $\beta(M)$ and $\chi(M)$, as well as their approximation by replacing $M(\boldsymbol{x}, t)$ with M_∞ and/or $\overline{M}$, suggest that, in an idealized compressible flow where the three processes were fully decoupled and free from highly nonlinear structures, each process would develop independently of the others, and these universal factors would fully modulate their respective variations as the local Mach number changes.

In addition to the universal factors, however, in real viscous and nonlinear compressible complex flow there must appear various specific Mach-number-dependent events associated with the birth, enhancement, suppression, or elimination of specific flow structures due to the self-nonlinearity of each process and their mutual coupling. These special events may alter the LT-force to different extents, but are crucially dependent on specific body geometry and initial-boundary conditions. They can by no means be characterized by simple factors like α or β. The more that the Mach-number dependence of the LT-force deviates from those universal factors, the stronger will specific structures and flow complexity be. The two types of Mach-number dependence, universal and specific, have both been observed as stated in §§ 5.1 and 5.2. Distinguishing these types is of considerable significance in practical applications.

6. Conclusions

The main preliminary findings of this paper can be summarized as follows.

(i) The incompressible unsteady vortex-force theory is fully generalized to the realm of compressible unsteady flow, yielding innovative integral formulae for the total force and moment acting on a body that can move/deform arbitrarily in the fluid. In addition to the T-force due to the shearing process and dominated by the Mach-number-weighted Lamb vector $\alpha(M)\boldsymbol{\omega} \times \boldsymbol{u}$ per unit mass, an L-force appears, including but not confined to supersonic wave drag, which is due to a compressing–thermodynamic process and dominated by $\beta(M)R\nabla[\alpha(M)T]$ per unit mass. The three processes are coupled with and modulate each other in an M-dependent manner. The new LT-force theory represents an advance in high-speed aerodynamic force theory from a classic inviscid and irrotational simple-flow model to viscous multi-process complex flow. Although the present theory is specific to laminar flow of calorically perfect gas with constant dynamic viscosity, it has opened a promising route to be extended to turbulent flow of real gas.

https://doi.org/10.1017/jfm.2014.403 Published online by Cambridge University Press

(ii) The new LT-force theory is confirmed by a high-fidelity numerical simulation of laminar flow over a two-dimensional circular cylinder with free-stream Mach number M_∞ ranging from 0.2 to 2.0. The division into an L-force and a T-force becomes R-independent if R, the radius of the diagnosis domain, is large enough, since then all flow structures are in the diagnosis domain and surface integrals vanish. The flow transforms from unsteady to quasi-steady at a critical $M_{cr} \approx 0.9$.

(iii) Combined with numerical Navier–Stokes solutions of complex compressible flow, the LT-force theory permits a detailed diagnosis of the respective contributions of longitudinal and transverse processes to the LT-force in a properly chosen analysis domain (which can be much smaller than the computational domain), by displaying their variations with the free-stream Mach number. Guided by the LT-force theory, it is found that for the time-averaged LT-drag acting on the cylinder, the longitudinal process can strongly modulate the evolution of vortical structures as M_∞ varies. It suppresses the wake vortex street and associated flow unsteadiness in the transonic regime and even eliminates them in the supersonic regime. But the inverse modulation is much weaker. The modulation of the T-force by the longitudinal process is analysed by the cross-modulation in the Lamb vector, as well as by the boundary vorticity flux and boundary vorticity. Although the self-nonlinearity of the Lamb vector turns the pure shearing vortex force into a thrust at $M_\infty \approx 0.7$, its cross-modulation part is strong enough to keep the total drag from the Lamb vector always positive. The magnitude of the peak values of BVF and BV decrease monotonically as M_∞ increases.

(iv) The Mach-number dependence of complex flow has both a specific aspect and a universal aspect. The former is strongly influenced by the body geometry, initial-boundary conditions, and evolution of various flow structures, while the latter is reflected by the appearance of universal local Mach-number factors that are derived solely from basic governing equations, such as factors $\alpha(M)$, $\beta(M)$, $\chi(M)$ and $\zeta(M)$. In the time-averaged steady flow, if the local Mach number $M(\boldsymbol{x}, t)$ could be approximated by constant M_∞ plus a space-averaged $\overline{M}$ which may differ from M_∞ significantly in complex flow, there would be a possibility of expressing the force approximately by that at a reference M_∞ (say, $M_\infty = 0$ or 2) times a factor of M_∞ and/or $\overline{M}$. As a preliminary study for the circular-cylinder flow, we sought this possibility by a linear combination of the two constant Mach numbers with coefficients being determined by curve fitting. The results are surprisingly promising: except for $\overline{C}_{d,\boldsymbol{\omega}\times\boldsymbol{u}}$, which is dominated by the very complex wake vortical flow in the subsonic regime, other major constituents of $\overline{C}_{d,L}$ and $\overline{C}_{d,T}$ can be closely mimicked by $\beta(M_\infty)$, $\beta(\overline{M})$, and $\chi(M_\infty)$ even in the transonic regime, with only a minor error around M_{cr}. This numerical experiment could serve as a starting point of a more rational search for new similarity rules for the L-force and T-force.

Acknowledgements

This work was supported by NSFC (grant no. 10921202) and MOST (project no. 2009CB724100) of China. The numerical computation was partially carried out at the National Supercomputer Center in Tianjin, with calculations performed on TianHe-1(A). The authors are very grateful to Professors B.-G. Tong, H.-X. Zhang, S.-H. Zhang, X.-L. Li, X.-Y. Lu, F. Liu, C.-J. Wu, Y.-L. Yu and L. Bao, and Drs L.-J. Xuan, F. Mao and Z.-J. Liao, for valuable discussions.

https://doi.org/10.1017/jfm.2014.403 Published online by Cambridge University Press

REFERENCES

BURGERS, J. M. 1921 On the resistance of fluids and vortex motion. *Koninklijke Nederlandse Akademie van Wetenschappen Proceedings Series B Physical Sciences* **23**, 774–782.

CHANG, C. C. & LEI, S. Y. 1996 On the sources of aerodynamic forces: steady flow around a cylinder or a sphere. *Proc. R. Soc. Lond.* A **452**, 2369–2395.

CHANG, C. C., SU, J. Y. & LEI, S. Y. 1998 On aerodynamic forces for viscous compressible flow. *Theor. Comput. Fluid Dyn.* **10**, 71–90.

CHU, B. T. & KOVÁSZNAY, L. S. G. 1958 Non-linear interactions in a viscous heat conducting compressible gas. *J. Fluid Mech.* **3**, 494–514.

FIABANE, L., GOHLKE, M. M. & CADOT, O. 2011 Characterization of flow contributions to drag and lift of a circular cylinder using a volume expression of the fluid force. *Eur. J. Mech. (B/Fluids)* **30**, 311–315.

GILBARG, D. & PAOLUCCI, D. 1953 The structure of shock waves in the continuum theory of fluids. *J. Rat. Mech. Anal.* **2**, 617–642.

HUANG, G. C. 1994 *Unsteady Vortical Aerodynamics: Theory and Applications*. Shanghai Jiaotong University Press, (in Chinese).

VON KÁRMÁN, TH. 1941 Compressibility effects in aerodynamics. *J. Aero. Sci.* **8**, 337–356.

VON KÁRMÁN, TH. & SEARS, W. R. 1938 Airfoil theory for non-uniform motion. *J. Aeronaut. Sci.* **5**, 379–390.

KOVÁSZNAY, L. S. G. 1953 Turbulence in supersonic flow. *J. Aero. Sci.* **20**, 657–674.

LAGERSTROM, P. A. 1964 *Laminar Flow Theory*. Princeton University Press.

LAGERSTROM, P. A., COLE, J. D. & TRILLING, L. 1948 Problems in the theory of viscous compressible fluids. *GALCIT Tech Rep.* 6.

LI, G. J. & LU, X. Y. 2012 Force and power of flapping plates in a fluid. *J. Fluid Mech.* **712**, 598–613.

LIU, L. Q., WU, J. Z., SHI, Y. P. & ZHU, J. Y. 2014 A dynamic counterpart of Lamb vector in viscous compressible aerodynamics. *Fluid Dyn. Res.* (in press).

LUO, Y. B. 2004 Boundary vorticity dynamics, derivative moment theory, and their applications in flow diagnosis and control. Master thesis, Peking University.

MAO, F., SHI, Y. P. & WU, J. Z. 2010 On a general theory for compressing process and aeroacoustics: linear analysis. *Acta Mechanica Sin.* **26**, 355–364.

MAO, F., SHI, Y. P., XUAN, L. J., SU, W. D. & WU, J. Z. 2011 On the governing equations for the compressing process and its coupling with other processes. *Sci. China. Phys. Mech. Astron.* **54**, 1154–1167.

MARONGIU, C. & TOGNACCINI, R. 2010 Far-field analysis of the aerodynamic force by Lamb vector integrals. *AIAA J.* **48**, 2543–2555.

MARONGIU, C., TOGNACCINI, R. & UENO, M. 2013 Lift and lift-induced drag computation by Lamb vector integration. *AIAA J.* **51**, 1420–1430.

MCCUNE, J. E. & TAVARES, T. S. 1993 Perspective: unsteady wing theory—the Kármán/Sears legacy. *J. Fluids Engng* **115**, 548–560.

MELE, B. & TOGNACCINI, R. 2014 Aerodynamic force by Lamb vector integrals in compressible flow. *Phys. Fluids* **26**, 056104.

OSWATITSCH, K. 1956 *Gas Dynamics*. Academic.

PIERCE, A. D. 1989 *Acoustics: An Introduction to its Physical Principles and Applications*. Acoustical Society of America.

PRANDTL, L. 1918 Nachrichten von der Gesellschaft der Wissenschaften zu Göttingen, Mathematisch-Physikalische Klasse. *Tragflügeltheorie. I. Mitteilung*, pp. 451–477.

SAFFMAN, P. G. 1992 *Vortex Dynamics*. Cambridge University Press.

SHERMAN, F. S. 1955 A low-density wind-tunnel study of shock structure and relaxation phenomena in gases. *NACA Tech Rep.* 3298.

WU, J. C. 1981 Theory for aerodynamic force and moment in viscous flows. *AIAA J.* **19**, 432–441.

WU, J. Z., LU, X. Y., YANG, Y. T. & ZHANG, R. K. 2010 Vorticity dynamics in complex flow diagnosis and management. Pei-Yuan Chou memorial lecture. In *Proceedings 13th Asian Congr. Fluid Mech. Bangladesh Society of Mechanical Engineering, Dhaka* (ed. A. K. M. Sadrul Islam), pp. 19–38.

https://doi.org/10.1017/jfm.2014.403 Published online by Cambridge University Press

WU, J. Z., LU, X. Y. & ZHUANG, L. X. 2007 Integral force acting on a body due to local flow structures. *J. Fluid Mech.* **576**, 265–286.

WU, J. Z., MA, H. Y. & ZHOU, M. D. 2006 *Vorticity and Vortex Dynamics*. Springer.

WU, J. Z. & WU, J. M. 1993 Interactions between a solid surface and a viscous compressible flow field. *J. Fluid Mech.* **254**, 183–211.

WU, J. Z. & WU, J. M. 1996 Vorticity dynamics on boundaries. *Adv. Appl. Mech.* **32**, 19–275.

WU, J. Z., WU, H. & LI, Q. S. 2009 Boundary vorticity flux and engineering flow management. *Adv. Appl. Math. Mech.* **1**, 353–366.

WU, J. Z., WU, J. M. & WU, C. J. 1988 A viscous compressible flow theory on the interaction between moving bodies and flow field in the $(\boldsymbol{\omega}, \vartheta)$ framework. *Fluid Dyn. Res.* **3**, 203–208.

WU, T. Y. 1956 Small perturbations in the unsteady flow of a compressible, viscous and heat-conducting fluid. *J. Math. Phys.* **35**, 13–27.

WU, T. Y. 2007 A nonlinear theory for a flexible unsteady wing. *J. Engng Maths* **58**, 279–287.

XU, C. Y., CHEN, L. W. & LU, X. Y. 2009 Effect of mach number on transonic flow past a circular cylinder. *Chin. Sci. Bull.* **54**, 1886–1893.

XU, C. Y., CHEN, L. W. & LU, X. Y. 2010 Large-eddy simulation of the compressible flow past a wavy cylinder. *J. Fluid Mech.* **665**, 238–273.

YANG, Y. T., ZHANG, R. K., AN, Y. R. & WU, J. Z. 2007 Steady vortex force theory and slender-wing flow diagnosis. *Acta Mechanica Sin.* **23**, 609–619.

https://doi.org/10.1017/jfm.2014.403 Published online by Cambridge University Press